High-speed three-dimensional human retinal imaging by line-field spectral domain optical coherence tomography

著者	Nakamura Yoshifumi, Makita Shuichi, Yamanari Masahiro, Itoh Masahide, Yatagai Toyohiko, Yasuno Yoshiaki
journal or publication title	Optics Express
volume	15
number	12
page range	7103-7116
year	2007-05
権利	(C) 2007 Optical Society of America
URL	http://hdl.handle.net/2241/108171

doi: 10.1364/OE.15.007103

High-speed three-dimensional human retinal imaging by line-field spectral domain optical coherence tomography

Yoshifumi Nakamura[1], Shuichi Makita[1], Masahiro Yamanari[1], Masahide Itoh[2], Toyohiko Yatagai[2], and Yoshiaki Yasuno[1]*

[1]*Computational Optics Group in University of Tsukuba, Tsukuba, Ibaraki, Japan*

[2]*Institute of Applied Physics, University of Tsukuba, Tsukuba, Ibaraki, Japan*

yasuno@optlab2.bk.tsukuba.ac.jp

http//:optics.bk.tsukuba.ac.jp/COG/

Abstract: Line-field spectral domain optical coherence tomography (LF-SDOCT) has been developed for very high-speed three-dimensional (3D) retinal imaging. By this technique, the A-line rate significantly improved to 823,200 A-lines/s for single frame imaging and 51,500 A-lines/s for continues frame imaging. The frame rate at continues frame imaging is 201 fps. This 3D acquisition speed is more than two fold higher acquisition speed than the standard flying spot SD-OCT. In this paper, the integration time of the camera was optimized for the *in vivo* retinal measurement and the degradation of the lateral resolution due to the ocular aberrations was suppressed by introducing the pupil stop. Owing to an optimal integration time, the motion artifact can be significantly suppressed. Also a pupil stop was employed in order to enhance the contrast of the OCT image for the effect of ocular aberrations. The *in vivo* 3D retinal imaging with 256 cross-sectional images (256 A-lines/image) was successfully performed in 1.3 seconds, corresponding to 0.8 volume/s. The maximum on-axis system sensitivity was measured to be 89.4 dB at a depth of 112 μm with an axial resolution of 7.4 μm in tissue. It is shown that LF-SDOCT might have a sensitivity advantage in comparison to the flying spot SD-OCT in the ultra high-speed acquisition mode.

OCIS codes: (110.4500) Optical coherence tomography; (170.4500) Optical coherence tomography; (110.6880) Three-dimensional image acquisition; (170.4470) Ophthalmology.

References and links

1. D. Huang, E. A. Swanson, C. P. Lin, J. S. Schuman, W. G. Stinson, W. Chang, M. R. Hee, T. Flotte, K. Gregory, C. A. Puliafito, and J. G. Fujimoto, "Optical coherence tomography, Science **254**, 1178-1181 (1991).
2. G. Hausler and M. W. Lindner, ""Coherence radar"and"spectral radar"-new tools for dermatological diagnosis," J. Biomed. Opt. **3**, 21-31 (1998).
3. R. Leitgeb, C. Hitzenberger, and A. Fercher, "Performance of fourier domain vs. time domain optical coherence tomography," Opt. Express **11**, 889-894 (2003).
4. J. F. de Boer, B. Cense, B. H. Park, M. C. Pierce, G. J. Tearney, and B. E. Bouma, "Improved signal-to-noise ratio in spectral-domain compared with time-domain optical coherence tomography," Opt. Lett. **28**, 2067-2069 (2003).

#80474 - $15.00 USD Received 27 Feb 2007; revised 23 Apr 2007; accepted 26 Apr 2007; published 29 May 2007

5. N. Nassif, B. Cense, B. Park, M. Pierce, S. Yun, B. Bouma, G. Tearney, T. Chen, and J. de Boer, "In vivo high-resolution video-rate spectral-domain optical coherence tomography of the human retina and optic nerve," Opt. Express **12**, 367-376 (2004).
6. M. Wojtkowski, T. Bajraszewski, P. Targowski, and A. Kowalczyk, "Real-time in vivo imaging by high-speed spectral optical coherence tomography," Opt. Lett. **28**, 1745-1747 (2003).
7. M. Wojtkowski, V. Srinivasan, J. G. Fujimoto, T. Ko, J. S. Schuman, A. Kowalczyk and J. S. Duker, "Three-dimensional Retinal Imaging with High-Speed Ultrahigh-Resolution Optical Coherence Tomography," Ophthalmology **112**, 1734-1746 (2005).
8. M. Mujat, R. Chan, B. Cense, B. Park, Chulmin Joo, T. Akkin, T. Chen, and J. de Boer, "Retinal nerve fiber layer thickness map determined from optical coherence tomography images," Opt. Express **13**, 9480-9491 (2005).
9. S. Makita, Y. Hong, M. Yamanari, T. Yatagai, and Y. Yasuno, "Optical coherence angiography," Opt. Express **14**, 7821-7840 (2006).
10. S. Jiao, C. Wu, R. W. Knighton, G. Gregori, and C. A. Puliafito, "Registration of high-density cross sectional images to the fundus image in spectral-domain ophthalmic optical coherence tomography," Opt. Express **14**, 3368-3376 (2006).
11. S. Bourquin, P. Seitz, and R. P. Salathe, "Optical coherence topography based on a two-dimensional smart detector array," Opt. Lett. **26**, 512-514 (2001).
12. M. Laubscher, M. Ducros, B. Karamata, T. Lasser, and R. Salathe, "Video-rate three-dimensional optical coherence tomography," Opt. Express **10**, 429-435 (2002).
13. M. Lebec, L. Blanchot, H. Saint-Jalmes, E. Beaurepaire, and A. C. Boccara, "Full-field optical coherence microscopy," Opt. Lett. **23**, 244-246 (1998).
14. M. Akiba, K. P. Chan, and N. Tanno, "Full-field optical coherence tomography by two-dimensional heterodyne detection with a pair of CCD camera," Opt. Lett. **28**, 816-818 (2003).
15. W. Y. Oh, B. E. Bouma, N. Iftimia, R. Yelin, and G. J. Tearney "Spectrally-modulated full-field optical coherence microscopy for ultrahigh-resolution endoscopic imaging," Opt. Express **14**, 8675-8684 (2006).
16. I. Zeylikovich, A. Gilerson, and R. R. Alfano, "Nonmechanical grating-generated scanning coherence microscopy," Opt. Lett. **23**, 1797-1799 (1998).
17. Y. Watanabe, K. Yamada, and M. Sato, "In vivo nonmechanical scanning grating-generated optical coherence tomography using an InGaAs digital camera," Opt. Commun. **261**, 376-380 (2006).
18. Y. Watanabe, K. Yamada, and M. Sato, "Three-dimensional imaging by ultrahigh-speed axial-lateral parallel time domain optical coherence tomography,"Opt. Express **14**, 5201-5209 (2006).
19. A. Zuluaga and R. Richards-Kortum, "Spatially resolved spectral interferometry for determination of subsurface structure," Opt. Lett. **24**, 519-521 (1999).
20. B. Grajciar, M. Pircher, A. Fercher, and R. Leitgeb, "Parallel Fourier domain optical coherence tomography for in vivo measurement of the human eye," Opt. Express **13**, 1131-1137 (2005).
21. Y. Zhang, J. Rha, R. Jonnal, and D. Miller, "Adaptive optics parallel spectral domain optical coherence tomography for imaging the living retina," Opt. Express **13**, 4792-4811 (2005), http://www.opticsinfobase.org/abstract.cfm?id=84362.
22. T. Endo, Y. Yasuno, S. Makita, M. Itoh, and T. Yatagai, "Profilometry with line-field Fourier-domain interferometry," Opt. Express **13**, 695-701 (2005).
23. Y. Yasuno, T. Endo, S. Makita, G. Aoki, M. Itoh, and T. Yatagai, "Three-dimensional line-field Fourier domain optical coherence tomography for in vivo dermatological investigation," J. Biomed. Opt. **11**, 014014-014020 (2006).
24. American National Standards Institute, *American National Standard for Safe Use of Lasers: ANSI Z136.1* (Laser Institute of America, Orlando, Florida, 2000).
25. M. Takeda, H. Ina, and S. Kobayashi,"Fourier-transform method of fringe-pattern analysis for computer-based topography and interferometry,"J. Opt. Soc. Am. **72**, 156-160 (1982).
26. Y. Yasuno, V. D. Madjarova, S. Makita, M. Akiba, A. Morosawa, C. Chong, T. Sakai, K. -P. Chan, M. Itoh, and T. Yatagai,"Three-dimensional and high-speed swept-source optical coherence tomography for in vivo investigation of human anterior eye segments,"Opt. Express **13**, 10652-10664 (2005).
27. R. Leitgeb, W. Drexler, A. Unterhuber, B. Hermann, T. Bajraszewski, T. Le, A. Stingl, and A. Fercher, "Ultrahigh resolution Fourier domain optical coherence tomography," Opt. Express **12**, 2156-2165 (2004).
28. S. H. Yun, G. Tearney, J. de Boer, and B. Bouma, "Motion artifacts in optical coherence tomography with frequency-domain ranging," Opt. Express **12**, 2977-2998 (2004), http://www.opticsinfobase.org/abstract.cfm?id=80320.
29. S. H. Yun, G. Tearney, J. de Boer, and B. Bouma, "Pulsed-source and swept-source spectral-domain optical coherence tomography with reduced motion artifacts,"Opt. Express **12**, 5614-5624 (2004).
30. Zawadzki, S. Jones, S. Olivier, M. Zhao, B. Bower, J. Izatt, S. Choi, S. Laut, and J. Werner, "Adaptive-optics optical coherence tomography for high-resolution and high-speed 3D retinal in vivo imaging," Opt. Express **13**, 8532-8546 (2005).
31. B. Hermann, E. J. Fernandez, A. Unterhuber, H. Sattmann, A. F. Fercher, and W. Drexler, P. M. Prieto and P. Artal, "Adaptive-optics ultrahigh-resolution optical coherence tomography," Opt. Lett. **29**, 2142-2144 (2004).

#80474 - $15.00 USD Received 27 Feb 2007; revised 23 Apr 2007; accepted 26 Apr 2007; published 29 May 2007

32. E. J. Fernandez, B. Povazay, B. Hermann, A. Unterhuber, H. Sattmann, P. M. Prieto, R. Leitgeb, P. Ahnelt, P. Artal, and W. Drexler, "Three dimensional adaptive optics ultrahigh-resolution optical coherence tomography using a liquid crystal spatial light modulator," Vision Res. **45**, 3432-3444 (2005).
33. E. J. Fernandez and W. Drexler, "Influence of ocular chromatic aberration and pupil size on transverse resolution in ophthalmic adaptive optics optical coherence tomography,"Opt. Express **13**, 8184-8197 (2005).
34. E. J. Fernandez, A. Unterhuber, B. Povazay, B. Hermann, P. Artal, and W. Drexler, "Chromatic aberration correction of the human eye for retinal imaging in the near infrared," Opt. Express **14**, 6213-6225 (2006), http://www.opticsinfobase.org/abstract.cfm?URI=oe-14-13-6213
35. W. J. Donnelly, and A. Roorda, "Optimal pupil size in the human eye for axial resolution," J. Opt. Soc. Am. A **20**, 2010-2015 (2003).
36. S. Yun, G. Tearney, B. Bouma, B. Park, and J. de Boer, "High-speed spectral-domain optical coherence tomography at 1.3 m wavelength," Opt. Express **11**, 3598-3604 (2003), http://www.opticsinfobase.org/abstract.cfm?id=78225.
37. D. X. Hammer, R. D. Ferguson, T. E. Bigelow, N. V. Iftimia, and R. H. Webb, "Line-scanning laser ophthalmoscope," J. Biomed. Opt. **11**, 041126 (2006).

1. Introduction

Optical coherence tomography (OCT) has emerged as a new and promising technique for high-resolution cross-sectional imaging [1]. Since OCT is a noninvasive and noncontact imaging modality with micrometer-scale axial resolution, it has been implemented for a variety of medical researches. Especially, OCT has become one of the most successful instruments in ophthalmic imaging for the diagnosis and screening of human retinal diseases.

Recently, a modality for retinal OCT has been developed by using spectral domain OCT (SD-OCT) [2]. SD-OCT offers significant advantages in the detection sensitivity and image acquisition speed over the conventional time-domain OCT (TD-OCT) [3, 4]. It has been experimentally demonstrated that SD-OCT shows a 148-fold (21.7 dB) improvement in sensitivity over TD-OCT [5]. A higher image acquisition speed by SD-OCT has also been demonstrated with video-rate [5] and real-time [6] measurements.

The improvement in the speed of SD-OCT permits the three-dimensional (3D) imaging of the retinal structure *in vivo* [7]. This 3D visualization of the retinal structure has provided a potential of comprehensive and intuitive screening of retinal diseases. Further, several 3D image processing techniques have been demonstrated that enhance the visualization of the structure of a particular section of tissue [8, 9, 10].

In the 3D measurement by SD-OCT, however, two-dimensional (2D) mechanical scanning is mandatory, and the total number of axial profiles (A-line) in a certain period of time is fixed by the maximum line rate of the camera used in the system. Moreover, the image acquisition time is dominated by the time during which the patient can effectively focus the eye on a fixation target. As a result, the measurement of the highly dense 3D OCT data over a relatively large area is impractical due to eye motion, blinking, etc. Thus, an imaging modality for OCT with much higher speed is required for high dense 3D human retinal imaging.

A 2D parallel detection scheme with TD-OCT is one of the first trial for high-speed 3D measurements. Parallel TD-OCT techniques are categorized as transverse en-face oriented imaging methods and longitudinal cross-sectional oriented imaging methods. The former, which is referred to as full-field OCT (FF-OCT) or full-field optical coherence microscopy (FF-OCM), provides a transverse en-face image by employing wide-field illumination and a 2D area scan detector [11, 12, 13, 14, 15]. Several types of FF-OCT and FF-OCM have been demonstrated using 2D smart pixel silicon detector arrays [11, 12] and CCD cameras [13, 14, 15]. The depth structure of a sample is captured by the axial mechanical scanning of the reference arm.

The other configuration of 2D parallel TD-OCT is the longitudinal parallel TD-OCT, which produces a longitudinal cross-sectional image from a single captured image without mechanical scanning [16, 17, 18]. The longitudinal parallel OCT employs line-field illumination and a 2D

#80474 - $15.00 USD Received 27 Feb 2007; revised 23 Apr 2007; accepted 26 Apr 2007; published 29 May 2007

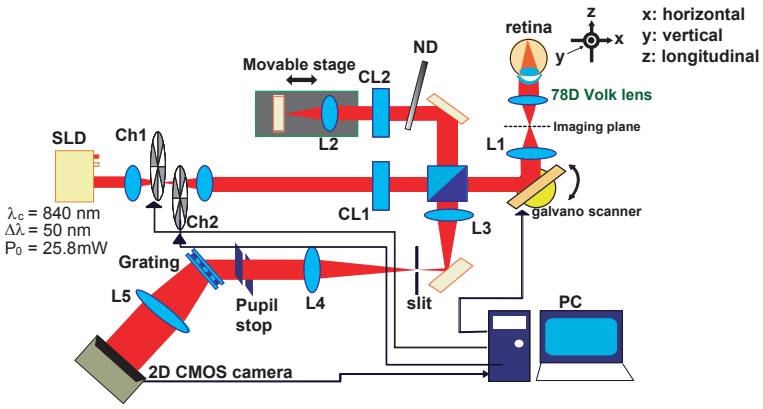

Fig. 1. Optical scheme of LF-SDOCT. SLD, superluminescent diode; L, Lens (L1, L2, L3, L4, and L5 are 60, 60, 100, 150, and 60 mm.); CL, cylindrical lens (CL1 and CL2 are 100 and 60 mm); Ch1 and Ch2, optical chopper; ND, nutral density filter.

detector. Recently, an *in vivo* 3D imaging of a human finger pad has been demonstrated at more than 1000 fps by using an ultra high-speed complementary metal oxide semiconductor (CMOS) camera [18]. However, since these parallel techniques are essentially based on the TD implementation of OCT, the use of the systems is restricted by a lower inherent sensitivity ($\leq$ 80 dB) than that of SD-OCT.

An alternative method for the longitudinal parallel TD-OCT has been demonstrated based on the SD implementation of OCT by Zuluaga et al [19]. Parallel SD-OCT is also performed with line illumination and a 2D area camera. The advantage of parallel SD-OCT over parallel TD-OCT is the sensitivity improvement that is exhibited at the same level as that in the conventional flying spot SD-OCT. Hence, parallel SD-OCT can potentially provide very high-speed, high-sensitivity 3D morphological imaging. In recent years, this technique has been applied to *in vivo* 2D anterior eye measurement [20] and *in vivo* 2D photoreceptor measurement combined with adaptive optics [21].

We have demonstrated line-field SD-OCT (LF-SDOCT) using this parallel SD-OCT technique for 3D metal surface profiling [22] and skin investigation [23]. In this study, we optimize LF-SDOCT for an *in vivo* 3D retinal imaging. By optimizing the camera integration time for the sample motion, the *in vivo* 3D human retinal structure was visualized at very high-speed, and the resulting images were sufficiently free of motion artifacts. To the best of our knowledge, this is the first demonstration of the visualization of *in vivo* 3D retinal imaging by LF-SDOCT technique.

2. System

2.1. Optical set-up

Figure 1 shows the optical scheme of our high-speed LF-SDOCT. In this scheme, the z-axis indicates the longitudinal direction of the system, and the x- and y-axes represent the horizontal and vertical transversal directions, respectively. Except for two cylindrical lenses and a 2D camera, the configuration is almost identical to that of the conventional flying spot free-space SD-OCT system.

The light source is a superluminescent diode (SLD) with the center wavelength of 840 nm and the FWHM bandwidth of 50 nm (S840-B-I-20, Superlum Diodes Ltd., Russia) which includes a built-in isolator. The output power from the single mode optical fiber pigtail is 26 mW. The

#80474 - $15.00 USD Received 27 Feb 2007; revised 23 Apr 2007; accepted 26 Apr 2007; published 29 May 2007

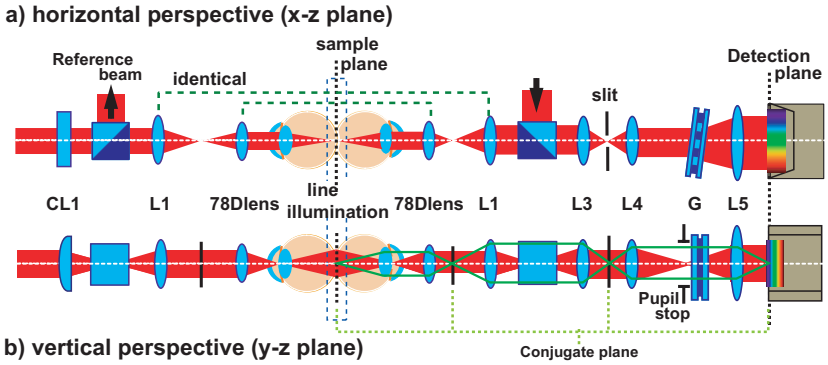

Fig. 2. Horizontal (a) and vertical (b) perspectives of the optical system. The two L1s and 78D lenses are identical. Cylindrical lens (L1) produces the line illumination on the sample. The sample plane is vertically conjugated with the detection plane.

axial resolution obtained experimentally is 7.4 μm in tissue (n = 1.38).

The collimated light is introduced into an expander to increase its FWHM beam diameter from 2.0 to 6.6 mm. In this expander, two optical choppers (MC1000A 10-slot-blade, Thorlabs Inc., USA) locate at the focal point in order to block the light during the read-out process of the camera; therefore, the sample is stroboscopically illuminated. The light through a cylindrical lens CL1 is divided by a nonpolarizing beam splitter into a probing beam and a reference beam. The insertion of the cylindrical lens CL1 produces a line-shaped probing beam in the sample arm, and a 78D lens was employed to focus the probe beam on the posterior of the eye. The vertically illuminating probe beam is estimated to be approximately 4.3 mm in length and 20.0 μm in width on the retina. On the other hand, the light in the reference arm is recollimated by a cylindrical lens CL2 again in order to make a movable optimum optical path length for various samples such as those for myopia, hyperopia, etc.

The light beams returning from the sample and reference arms are recombined collinearly and introduced into the spectrometer via relay lenses (L3 and L4). In the relay lenses, a slit is positioned at the conjugate plane of the sample in order to suppress the spatial coherent crosstalk due to the high spatial coherency of the light source, i.e., the SLD. Furthermore, a one-dimensional (1D) pupil stop with a size of 10.8 mm along the vertical y-z plane is placed in front of the grating, this is described in detail in section 3.2.

Figure 2 shows the horizontal and vertical perspectives of the system along the x-z and y-z planes in order to intuitively interpret the detection mechanism of LF-SDOCT. In the horizontal perspective, the wavelength-resolved interference signal is detected by the same mean as that used in the flying spot SD-OCT system. Namely, the light incident into the spectrometer is dispersed by a transparent grating (1200 lp/mm, Wasatch Photonics Inc., USA) and focused by an achromatic lens (f = 60 mm, Thorlabs Inc., USA) on a high-speed 2D CMOS area camera with effective pixels of 1104 (horizontal: H) $\times$ 256 (vertical: V) (12bit, ATMOS1M60, Atmel Corp., USA) and the pixel size of 5 μm. The horizontal pixels of the camera detect a 66 nm bandwidth centered at 840 nm where each pixel is separated by 0.061 nm. This sampling interval results in a theoretical axial measurement range of 2.90 mm. The actual measurement range was experimentally measured to be 2.88 mm, and this range agrees well with the theoretical value.

On the other hand, the optical configuration of the vertical perspective is different from that of the flying spot SD-OCT. The sample is illuminated by a line-shaped focusing beam. Since the sample plane is located at the conjugate plane of the camera, each vertical position of the

#80474 - $15.00 USD Received 27 Feb 2007; revised 23 Apr 2007; accepted 26 Apr 2007; published 29 May 2007

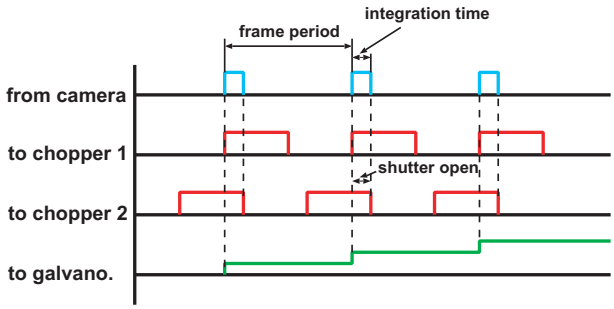

Fig. 3. Schematic representation of the synchronization time chart of LF-SDOCT. Both choppers are open, i.e., the sample is illuminated only during the integration time of the camera.

sample illuminated by the line-shaped probing beam is recorded on the corresponding vertical pixel of the camera by the imaging optics. The lateral vertical measurement range of 2.1 mm on the retina is determined by the imaging magnification of 0.61 and the active vertical chip size of 1.28 mm containing the number of 256 vertical pixels. Subsequently, a theoretical vertical lateral resolution of 16.4 μm along the imaging direction is estimated using the abovementioned magnification and a camera pixel size of 5 μm^2 by the Nyquist theorem. The optical diffraction limited vertical lateral resolution of 9.7 μm is also estimated and this is below that obtained by the Nyquist theorem. Hence, the vertical lateral resolution in our system is dominated by the Nyquist limit.

2.2. Synchronization

Since the CMOS camera used in our system operates in a rolling shutter mode and the maximum incident power on the eye is restricted by ANSI standard [24], light should be shut out externally when the camera is in the readout process. Figure 3 shows a schematic representation of the synchronization time chart. The two optical choppers and a one-axis galvanoscanner for volume data acquisition are synchronized by the trigger signals from the camera. The arbitrary integration time is produced by changing the relative phase of the signals driving the two optical choppers. In this study, the integration time is set at 311 μs; the reason for this is described in section 3.1. When the number of pixels is 1104 (H) $\times$ 256 (V) and the integration time is 311 μs, the driving speed of the camera is 201 fps. Hence, the sample is stroboscopically illuminated with the duration time of 311 μs, the repetition rate of 201 Hz, and the illumination power of 9.7 mW. It is corresponding to that the energy of each pulse on the sample is 3.0 μJ and the average probing power is 603 μW. This is below the ANSI standard of laser safety for the 840nm wavelength light source.

2.3. Post processing

The captured 2D spectrum that consists of 1104 (H) $\times$ 256 (V) pixels is transferred from the camera to a personal computer (Athlon 64 3500+ processor, 2 GB memory) via an image acquisition board (PCIe-1429, National Instruments Corp., USA). A custom software was developed in LabVIEW 8.0. First, the captured 2D spectrum is subtracted by a 2D averaged reference spectrum obtained from 40 successive 2D reference spectra. This averaging of the reference spectra cancels the mechanical jitter of the optical choppers that causes slight fluctuations of the light intensities incident into the camera. The subtracted 2D spectrum is divided by the normalized square root of a vertical 1D array which is obtained from horizontal integration of the 2D averaged reference spectrum. This is to removes the irregularities in the illumination

#80474 - $15.00 USD Received 27 Feb 2007; revised 23 Apr 2007; accepted 26 Apr 2007; published 29 May 2007

pattern. The divided spectrum is rescaled into the k-space using the spectral phase obtained by Fourier transform method [25, 26]. Thereafter, the residual 2nd and 3rd order dispersion unbalance between the reference and sample arms is numerically compensated. The compensated 2D spectrum is zero padded from 1104 to 2048 pixels along the horizontal direction in order to increase the sampling density in the time domain [27]. Finally, a cross-sectional image of 1024 (depth) $\times$ 256 (transverse) pixels is obtained by the horizontally Fourier transform.

3. Optimizations for retinal measurement

3.1. Integration time

In optical measurements, the shot noise limited signal-to-noise ratio (SNR) of the system increases with the integration time. The integration time of LF-SDOCT is longer than that of the conventional flying spot SD-OCT, because the system speed is restricted by the read-out time of the 2D camera. The duty cycle of our system is 6.25 %. The other groups that are developing a similar type of LF-SDOCT have adopted an integration time of 1 ms, while an integration time of approximately 50 μs is generally used for the conventional flying spot SD-OCT.

One of the significant problems that produces a critical signal distortion in SD-OCT is fringe washout due to sample motion [28, 29]. SD-OCT records the depth profile of the sample as the amplitude and the phase of the spatial frequency. The path length changes during a single A-line acquisition result in a phase drift in the interference fringe, causing a fringe washout. As a result, the fringe washout due to sample motion causes the loss of the signal, thereby resulting in the degradation of the SNR. Especially, in the case of *in vivo* 3D imaging with SD-OCT, sample motion is not negligible because of its long measurement time. In particular, this effect is more severe in LF-SDOCT because its single integration time is much longer than that of the flying spot SD-OCT and fringe washout affects the 2D spectrum obtained by one-shot of the camera rather than a single A-line. Hence, the fringe washout causes the severe image distortion, in which it appears like that a frame is missing. Therefore, it is important to determine the optimum integration time for *in vivo* human retinal measurement.

Yun et al. have determined the quantitative amount of signal degradation due to the axial motion of a sample in SD-OCT [28]. Since the problem of the lateral motion of a sample is not as critical as that of its axial motion, the former can be neglected. Then, the signal intensity degraded by axial motion is expressed as follows [28, 29]:

$$S(k) = S_0(k)\frac{\sin^2(k v_z \tau)}{(k v_z \tau)^2}, \tag{1}$$

where $S_0(k)$ denotes the signal intensity without axial motion, k is the center wavenumber, v_z is the axial velocity of the sample, and τ is the integration time. We assume that the axial velocity of the sample is 500 μm/s, which is the average measure of the axial motion estimated from the retinal 3D OCT data obtained by using our standard flying spot SD-OCT [9]. The main source of the motion could be assumed as the involuntary head movement. Figure 4 shows the theoretical shot noise limited sensitivity with and without the axial motion over the integration time. This graph indicates that the optimum sensitivity for *in vivo* retinal imaging can be obtained at an integration time of 311 μs.

To confirm this result experimentally, time sequences of the cross-sectional images were obtained at integration times of 1 ms and 311 μs as shown in Fig. 5. 256 cross-sectional images are captured within 2.5s without scanning the galvano scanner for each setting. These movies verify that the number of missing frames due to the sample motion can be dramatically reduced in the images acquired at 311 μs integration time.

In order to quantify these results, a sign-inverted information entropy of the images is derived

#80474 - $15.00 USD Received 27 Feb 2007; revised 23 Apr 2007; accepted 26 Apr 2007; published 29 May 2007

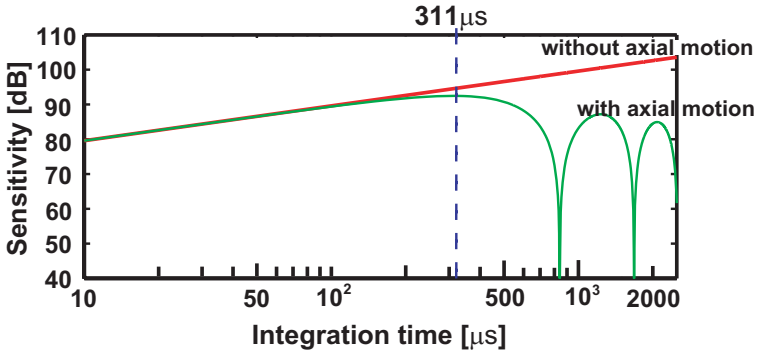

Fig. 4. Plot of the sensitivity with and without axial motion versus the integration time of the camera. Although the sensitivity without axial motion monotonously increases with the integration time, the maximum sensitivity with axial motion is obtained at an integration time of 311 μs.

Fig. 5. Image comparison between the integration times of (a) 1 ms and (b) 311 μs. The fringe washout affects the entire cross-sectional image. The shown representative image is 29th one in 256 successively captured cross-sectional image. A movie of the time sequence of the images are available for the comparison between with integration times of 1 ms and 311 μs (2.1 MB movie). Also, a version of 8.0 MB is available.

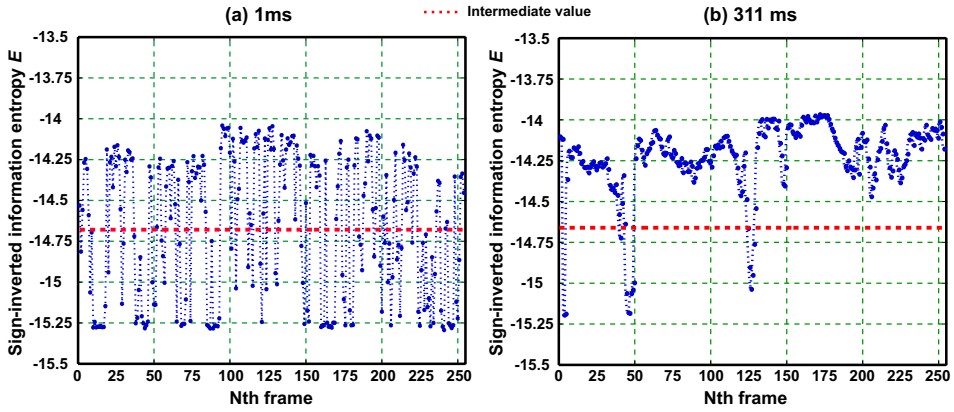

Fig. 6. Evaluation function of each frame for the integration times of (a) 1 ms and (b) 311 μs. The result obtained for 1ms shows a lot of missing frames due to the motion artifact in quantitative comparison to that for 311 μs .

#80474 - $15.00 USD Received 27 Feb 2007; revised 23 Apr 2007; accepted 26 Apr 2007; published 29 May 2007

as an evaluation function.

$$E = \sum_{z,y} \left(\frac{I(z,y)}{\sum I(z,y)} \right) \log_2 \left(\frac{I(z,y)}{\sum I(z,y)} \right), \tag{2}$$

where $I(z,y)$ represents a linear OCT signal intensity. This function is useful to evaluate a measure of the signal concentration in the image. The value of the evaluation function for each image is shown in Fig. 6. When the fringe washout occurs due to the sample motion, the value of the evaluation function rapidly decreases. The red dotted lines represent the intermediate value between the maximum and minimum values of the evaluation function. The number of the images with a value higher than the intermediate value is 139 and 239 for the integration times of 1 ms and 311 μs, respectively. The value of 239 corresponds to 93.3 % of the total number of the images, 256. This confirms that the effect of the motion artifact can be significantly suppressed by optimizing the integration time for *in vivo* retinal measurement.

Although in this simulation we have assumed that the velocity of the axial motion is always constant, this is not only the case in practice. Hence, this optimization method cannot overcome the problem of motion artifacts completely; however, its performance is reasonably high.

3.2. Ocular aberrations

Ocular aberrations cause wavefront aberrations, and they are one of the significant sources of image quality distortion in OCT. Wavefront aberrations comprise of monochromatic and chromatic aberrations. The correction of monochromatic ocular aberrations has been demonstrated by using an adaptive optics device in standard OCT [21, 30] and in ultra-high resolution (UHR) OCT [31, 32]. The use of a broadband light source is also mandatory in OCT. Hence, the chromatic aberration of the human eye is also a significant problem in OCT. Recently, the chromatic ocular aberrations in the near infrared (NIR) region of the spectrum have been mathematically modeled [33], and corrected using an achromatizing lens [34].

In the case of LF-SDOCT, the ocular aberrations considerably affect the image quality in comparison to that in the flying spot SD-OCT. Since LF-SDOCT employs imaging optics for the non-mechanical B-scan and simultaneously acquires all the A-lines in the single cross-sectional image, the aberrated light between the neighboring A-lines interfere with each other, and the consequential coherent crosstalk critically degrades the OCT image quality. An adaptive optics technique employing a Shack-Hartmann wavefront sensor and a deformable mirror has been used in the parallel SD-OCT technique [21]. However, adaptive optics makes the optical configuration elaborate and the practical lateral measurement range is limited into several hundred micrometers.

The simplest method to suppress the effect of ocular aberrations is the use of a pupil stop. Ocular aberrations are known to increase with the size of the pupil stop, while the spot size of the light focusing on the image plane increases as the pupil size decreases. Optimal pupil size for axial and lateral resolution was examined by Donnelly and Roorda [35]. In this study, we applied a pupil size of 1.8 mm on the cornea.

To confirm the effect of the pupil stop, a 2D retinal image is acquired with and without the pupil stop. In practice, a pupil stop with a size of 10.8 mm is placed in front of the grating, which is the conjugate point of the cornea in order to avoid the vignetting of the incident probing beam. The pupil size is calculated based on thepupil size of 1.8 mm on the cornea and an optical magnification of 6. Figure 7 verifies that the pupil stop clarifies several retinal layers and provides an image with a high contrast, particularly for the inner segment and outer segment junction (IS/OS).

#80474 - $15.00 USD Received 27 Feb 2007; revised 23 Apr 2007; accepted 26 Apr 2007; published 29 May 2007

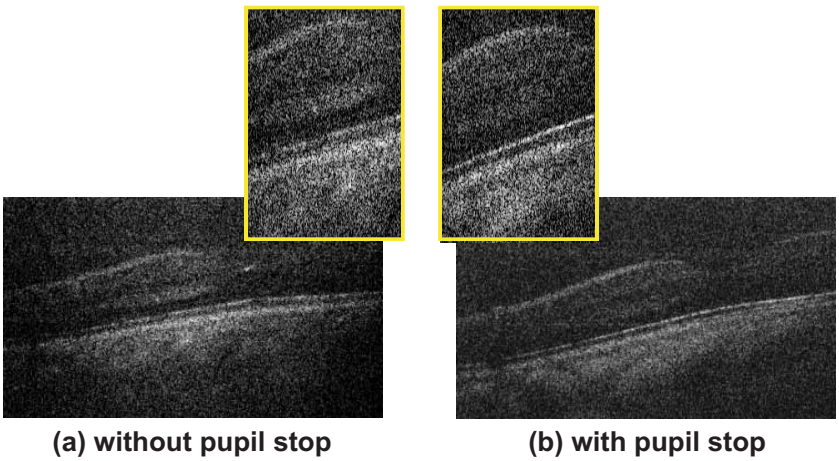

Fig. 7. Qualitative image comparison between the (a) absence and (b) presence of the pupil stop.

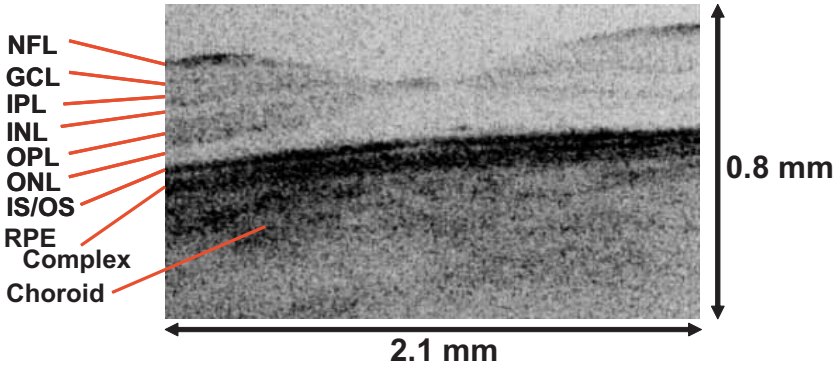

Fig. 8. Time sequence of the cross-sectional image for the macula of an *in vivo* human healthy volunteer (2.2 MB movie). Also, the version of 12.0 MB is available.

4. Result and discussions

4.1. In vivo high-speed 3D retinal imaging

In vivo 3D images of macula of a healthy volunteer were captured by LF-SDOCT. Figure 8 shows a time sequence of the cross-sectional images. Each image frame is constructed from 256 A-lines over an area of 2.1 mm on the retina. The vertically line-shaped probing beam was horizontally scanned around the fovea over an area of 2.3 mm from the nasal to the temporal, where 256 cross-sectional images were acquired during the scanning. A single cross-sectional image is acquired at 311 μs. Since the system provides a cross-sectional image acquisition speed of 201 fps, the total measurement time for the entire set of the 3D image data is 1.3 s.

After the 2D image processing described in section 2.3, the influence of the axial motion of the sample is compensated for the neighboring cross-sectional images by a simple correlation-based algorithm [9]. This compensation can be confirmed in Fig. 9 that shows the volume rendering image of Fig. 8. In addition to the motion compensation, a despeckle filter that composites several neighboring images is applied to Fig. 8 in order to enhance the contrast of each retinal layer.

#80474 - $15.00 USD Received 27 Feb 2007; revised 23 Apr 2007; accepted 26 Apr 2007; published 29 May 2007

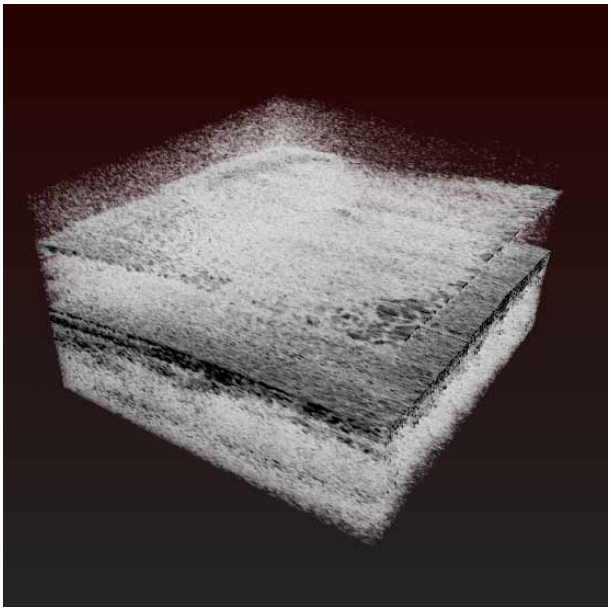

Fig. 9. Volume rendering image of the retina. The original data set is same as Fig. 8.

Several retinal layers such as the nerve fiber layer (NFL), ganglion cell layer (GCL), inner plexiform layer (IPL), inner nuclear layer (INL), outer plexiform layer (OPL), outer nuclear layer (ONL), IS/OS, retinal pigment epithelium (RPE) complex, and choroid are visible in the image. We can also see the external limiting membrane (ELM) in some images.

4.2. Sensitivity

4.2.1. Maximum on-axis sensitivity

The maximum sensitivity of the system is obtained at the central on-axis A-line in the single cross-sectional image because the line illumination on the sample has a Gaussian intensity profile. Hence, the theoretical maximum sensitivity at the central on-axis A-line is calculated.

The main noise sources in SD-OCT are the electrical noise N_{el} of the detector, shot noise N_{sh}, and optical intensity noise N_{IN}, where shot noise and optical intensity noise are dominated by the reference arm light [36]. An optimum shot noise limited sensitivity of our system will be obtained at N_{ref} = 124,600 electrons where $N_{el} = N_{IN}$. N_{ref} represents the number of electrons per pixel generated by only the optical power from the reference beam. However, the full well depth of our camera is 65,535 electrons and this is less than the number of electrons for the optimal shot noise limited sensitivity. Hence, the maximum sensitivity of the system is limited by the saturation-level of the camera. Based on this saturation-level, each noise of our system is calculated as N_{sh} = 233, N_{IN} = 39, and N_{el} = 88 electrons. Since shot noise is approximately two fold bigger than the other noises, The system sensitivity is dominated by the shot noise. The theoretical shot noise limited sensitivity is predicted as 95.9 dB by using the integration time of 311 μs, the beam splitter's splitting ratio of 0.5, and the spectrometer-camera quantum efficiency of 0.34. The sample illumination power corresponding to on-axis pixels is 17 μW, where the total sample illumination power is 9.7 mW and the intensity profile is Gaussian shape with the FWHM of 4.3 mm. And, the theoretical sensitivity considering three noises is estimated as 93.5 dB.

#80474 - $15.00 USD Received 27 Feb 2007; revised 23 Apr 2007; accepted 26 Apr 2007; published 29 May 2007

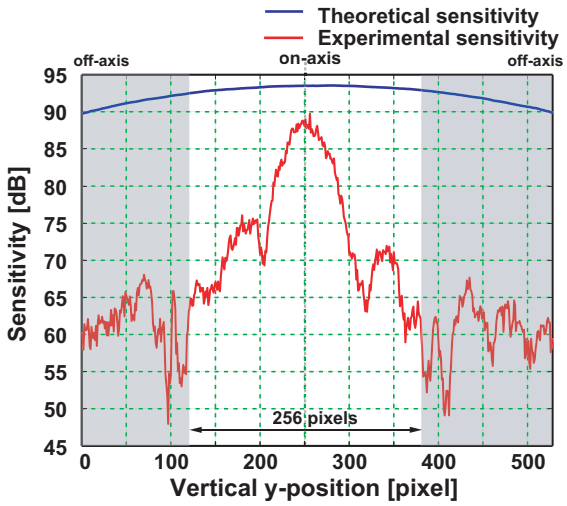

Fig. 10. Lateral position dependence of the sensitivity. Theoretical distribution of the sensitivity calculated from the Gaussian intensity profile of the line illumination on the sample (blue line). Experimental distribution of the sensitivity obtained using an achromatic lens and a mirror (red line).

The experimental sensitivity is measured using a simple practical eye model that consists of an f = 30 mm achromatic lens and a gold mirror. The reference optical power is adjusted by a neutral density (ND) filter so that the pixel values reach to approximately 90 % of the saturation level at each frame. Then, the experimental sensitivity of 89.4 dB was obtained at a depth of 112 μm in air with a -51.3 dB attenuation. The departure of approximately -4 dB from the theoretical prediction may be accounted by the rescaling error into the frequency linearity, the non-Gaussian spectral shape, and the Hamming window filtering applied to the spectrum before the Fourier transform. The sensitivity drops are -12 dB and -23 dB at a depth of 1.0 mm and 2.0 mm, respectively. This relatively large drop is due to low spectral resolution of the spectrometer and the small wavelength spacing. Since we are using the relatively small pixel size of the camera, it is hard to make a high spectral resolution.

4.2.2. Lateral vertical position dependence of sensitivity

Figure 10 shows the lateral position dependence of the sensitivity at a depth of 112 μm . The horizontal axis represents the y-position along the line illumination, i.e., the imaging direction. The on-axis position is located at approximately 250th pixel. This figure shows that the sensitivity significantly decreases as the y-position becomes distant from the on-axis point. The departure from the theoretical sensitivity is about -30 dB at the edge of the measurement range. This kind of sensitivity degradation is also observed in a similar system demonstrated by other group [21]. This degradation in the sensitivity may be accounted by the spatial coherence crosstalk derived from the aberrations, the tolerance, and the extent of the spot size described later.

In practice, central 256 pixels are used as the number of effective pixels for 3D human retinal imaging for the high-speed acquisition because there is a trade-off between the number of active pixels and the frame rate in the camera.

#80474 - $15.00 USD Received 27 Feb 2007; revised 23 Apr 2007; accepted 26 Apr 2007; published 29 May 2007

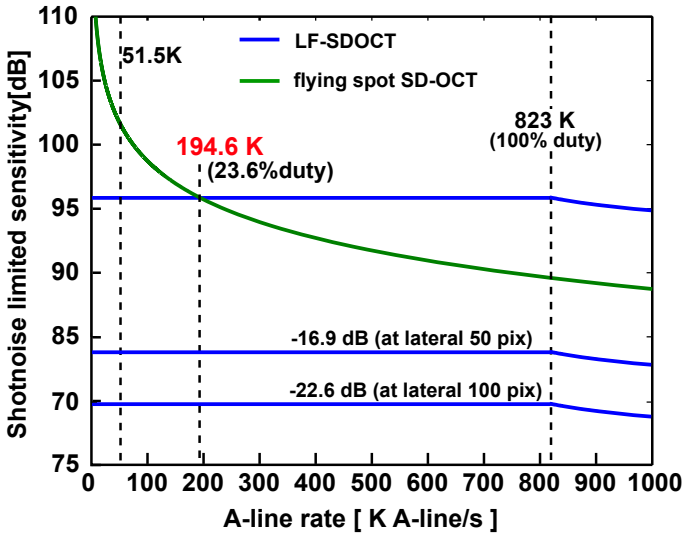

Fig. 11. Change in the sensitivity property with the increase in the A-line rate. The sensitivity for the flying spot SD-OCT that attains a 100 % duty cycle (green line). LF-SDOCT has a constant sensitivity until the system attains a 100 % duty cycle (red line). The flying spot SD-OCT used in this simulation is standard one which has the center wavelength of 840 nm, the probing power of 733 μW , the splitting ratio from the sample arm to the spectrometer of 0.8, and the spectrometer efficiency of 0.3. The degraded sensitivities of LF-SDOCT at lateral 50 and 100 pixels are also plotted.

4.3. Sensitivity advantage in ultra high-speed acquisition

LF-SDOCT offers higher-speed *in vivo* imaging of retina than the standard flying spot SD-OCT. Since a single cross-sectional image is acquired at 311 μs which is equal to the integration time of the camera, our system virtually provides 823,151 A-lines/s for the single frame imaging, corresponding to the reciprocal of the single integration time. For the 3D measurement, however, the A-line rate of the system reduces to 51,456 A-lines/s because the acquisition speed is restricted by the readout time of the camera. Even though, the A-scan rate of 51,456 in the 3D measurement is still approximately 2.6 times higher than that in the standard flying spot SD-OCT ($\simeq$20 K A-lines/s).

There are two factors to explain more attractive feature of LF-SDOCT. One is the probing power. In this experiment, 603 μW of the average probing power was employed in accordance with ANSI safety standard for point illumination in flying spot SD-OCT. However, in practice, LF-SDOCT uses line illumination, i.e., we can consider it as an extended source. Hence, the limitation of the incident light into the human eye is not as stringent as that of flying spot SD-OCT. According to the description for non-circular illumination in ANSI by using the parameter of the FWHM line length of 4.3 mm, the line width of 20 μm and the quasi angular subtense of 25.9 mrad calculated from the illumination dimension, our configuration permits 10.9 mW of a maximum permissible incident power into the human eye [37]. The other factor is also the duty cycle. At present, our system attains only a 6.25 % duty cycle because the acquisition speed is almost restricted by the readout time. On the other hand, the standard flying spot SD-OCT nearly reaches to a 100 % duty cycle. Hence, the future improvement of the data transfer speed from the camera allows ultra high-speed LF-SDOCT while maintaining the sensitivity.

Figure 11 shows the dependence of sensitivity on the A-line acquisition rate. The sensitivity

#80474 - $15.00 USD Received 27 Feb 2007; revised 23 Apr 2007; accepted 26 Apr 2007; published 29 May 2007

remains constant with an increase in the acquisition speed in LF-SDOCT until 100 % duty cycle is attained. The constant sample illumination power of 10.9 mW is set, which means that the average probing power is smaller when the duty cycle is less than 100 %. On the other hand, the sensitivity in the flying spot SD-OCT decreases as the A-line rate increases since the high-speed acquisition is restricted by the integration time. Hence, the improvement of the high-speed acquisition results in the decrease of the sensitivity accompanied by the limitation of the integration time. This graph shows that the sensitivity in LF-SDOCT becomes higher than that of the flying spot SD-OCT over 195 K A-line/s. However, the sensitivity degrades along the lateral direction as shown in Fig. 10. The sensitivity decay at 50 and 100 pixels from the center was -16.9 dB and -22.6 dB, respectively, by averaging decays on both side. The degraded sensitivity is also depicted in Fig. 11. The lateral sensitivity decay is the disadvantage of the LF-SDOCT. If it is solved in future, the LF-SDOCT has an potential to achieve higher sensitivity than that of the flying spot SD-OCT with high A-line rate.

5. Conclusion

We have demonstrated LF-SDOCT for the application of 3D high-speed human retinal imaging. This OCT virtually has the measurement speed of 51,500 A-lines/s for the 3D imaging, which is over two-fold higher than that of the conventional flying spot SD-OCT. The optimal integration time of the camera for *in vivo* retinal measurement was estimated to be 311 μs by examining the signal degradation due to the axial motion of the human eye. Further, a pupil stop size of 1.8 mm on the cornea was set in order to suppress the effect of ocular aberrations, and it enhanced the image contrast of the retinal structure. The *in vivo* 3D human retinal imaging with 256 cross-sectional images (256 A-lines/image) was visualized in 1.3 seconds by optimized LF-SDOCT for the *in vivo* retinal measurement. This result revealed the potential of LF-SDOCT for high-speed retinal imaging. The maximum on-axis sensitivity in our system was also measured to be 89.4 dB with the axial resolution of 7.4 μm in tissue. We also found that the sensitivity rapidly degrade as far from on-axis point in the system. However, although this system still remains a problem of experimental improvement for the sensitivity degradations, the analysis of the sensitivity with an increase in the A-line rate shows that LF-SDOCT will have the possibility of ultra high-speed imaging with maintaining higher sensitivity than that in flying spot SD-OCT.

Acknowledgments

This research is partially supported by a Grant-in-Aid for Scientific Research (No. 15760026, No. 18360029) from the Japan Society for the Promotion of Science (JSPS), Japan Science and Technology Agency, and the Special Research Project of Nanoscience at the University of Tsukuba. S. Makita is supported by Research Fellowships of the Japan Society for the Promotion of Science for Young Scientists. M. Yamanari is partially supported by the MEXT through a contract under the Promotion of Creative Interdisciplinary Materials Science for Novel Functions, 21st Century Center of Excellence (COE) Program.

#80474 - $15.00 USD Received 27 Feb 2007; revised 23 Apr 2007; accepted 26 Apr 2007; published 29 May 2007